Quantitative Analysis of Doppler-Free Spectra via the Collisional-Radiative Model

Joseph John SIMONS[1)]*, Motoshi GOTO[1,2)], Tomoko KAWATE[1,2)], Shusuke NISHIYAMA[3)]

[1)] *Graduate University for Advanced Studies, SOKENDAI, Toki 509-5292, Japan*
[2)] *National Institute for Fusion Science, National Institutes of Natural Sciences, Toki 509-5292, Japan*
[3)] *Japan Healthcare University, Sapporo 062-0023, Japan*

(Received 26 August 2024 / Accepted 19 March 2025)

We have constructed a simulation model of the Doppler free spectra for the hydrogen Balmer α line. We are introducing the laser excitation process into the collisional-radiative model of hydrogen atoms to see how much saturation can be achieved under realistic plasma conditions and laser power density. Results show that the simulated spectra were able to successfully model Lamb dips and peaks utilizing this method, with the simulated plasma and laser parameters showing good agreement to the ones used in the experiment. This model has additionally helped illustrate further insight into how plasma parameters can affect the spectral characteristics of Lamb dips and peaks.

Keywords: saturated absorption spectroscopy, Doppler-free, collisional-radiative model, Lamb dip, Balmer alpha, fine structure

DOI: 10.1585/pfr.20.1401028

1. Introduction

Saturated absorption spectroscopy is an experimental technique that allows for precise determination of transition wavelengths typically between a lower atomic energy state and its more optically energetic states [1]. In order to make an example measurement of the saturated absorption profile of a transition line, a laser of a tunable wavelength is scanned over the entire line profile. Saturated absorption spectroscopy benefits from a much finer resolution than optical emission spectroscopy, and is thus prominently used in obtaining spectral distributions of various particles contained within plasma [2–7]. This is achieved by uncovering the desired transition line(s) from the Doppler-broadened spectra via dips in the spectra that occur at the location of the transition(s) in question known as Lamb dips. This results in the resolution of saturated absorption spectroscopy being primarily dictated by the width of the Lamb dips themselves. It is a widely used technique in the field of fundamental spectroscopy, where researchers are particularly interested in ultra-fine structures of various transition lines [8]. This particular method of overcoming Doppler broadening of the spectra is why this technique is also sometimes referred to as Doppler-free saturated absorption spectroscopy.

In this work the hydrogen Balmer-α line is focused on in particular due to the fact that this line is well understood and it contains a large number of fine structure components [9–11]. Previous work has shown that saturated absorption spectra of the *J*-resolved components of the hydrogen Balmer-α line demonstrate different characteristics depending on the discharge parameters of the plasma [12]. Such dependencies suggest that saturated absorption spectroscopy can be used as a tool for plasma diagnostics in high temperature plasmas. In order to do so however, we would first need to be able to model the characteristics of saturated absorption spectra as functions of the plasma discharge parameters. This would allow us to quantitatively analyze the spectra in a way that could determine the viability of saturated absorption spectroscopy as a diagnostic tool. The creation of such a model is the main motivation of this work.

In Sec. 2 of this paper we discuss the theory behind saturated absorption spectroscopy and the formation of Lamb dips. In Sec. 3 we then showcase how we are able to create a spectra model capable of obtaining the dependencies of spectral Lamb dips on various plasma parameters before going into more detail in Sec. 4 on the specifics of the collisional-radiative (CR) model used to generate the necessary energy level populations of particular particle velocity groups that are used to calculate the absorption coefficients of the spectrum. After briefly looking at the output of the CR model used in the theory in Sec. 5 we move to discuss the model's predictions of the spectral characteristics of Lamb dips as functions of laser power, electron density, atom and electron temperature independently. We then finish this paper with the conclusion in Sec. 6.

**Corresponding author's e-mail: josephjohn.simons@nifs.ac.jp*

2. Saturated Absorption Spectroscopy

2.1 Lamb dip formation

As previously stated, the key to saturated absorption spectroscopy's ability to produce Doppler-free spectral resolutions lies in its creation of Lamb dips that occur at transition frequencies of the atoms within the plasma. Let us take a look at how the formation of Lamb dips results in a Doppler-free spectrum. As shown in Fig. 1, an optical pump laser beam is injected into the plasma counter to a probe laser beam, with both beams originating from the same source but with differing intensities.

With this in mind let us imagine a wavelength that corresponds to a transition from lower energy level $|p\rangle$ to upper energy level $|q\rangle$. Due to the random thermal motion of atoms within a plasma, the reference point of an atom that contains a velocity v parallel to the propagation axis of both lasers would see that the pump and probe lasers would have different wavelengths due to an effect known as Doppler shifting. Since the pump and probe lasers would have different wavelengths in the atom's frame of reference, if the atom resonates with either the pump or the probe laser wavelength, it does not resonate with the other beam unless the component of the velocity along the laser axis is zero. This means that there is no change in the absorption due to the particles at that particular velocity.

If the atom has no velocity component parallel to the laser axis however, no Doppler shift occurs and both the pump and probe beams maintain the same wavelength from the atom's point of view. In this scenario, the pump beam and probe beam are now interacting with the same group of particles. This means that electrons are pumped into the upper excited level associated with the transition frequency resonant with the beams until the population is saturated. The probe beam then has a greatly increased chance of encountering these excited atoms and releasing photons via stimulated emission as the atoms relax back into the lower energy state. A dip in the absorption is thus formed at the line center of the Doppler-broadened spectrum as a result of this process. This dip is called the Lamb dip, and with it the saturation spectrum obtains a Doppler-free resolution.

The plotted orange spectrum in Fig. 2 is an example of the hydrogen Balmer-α line spectrum measured for an inductively coupled plasma (ICP) source produced with an RF power of 1 kW and an RF frequency of 13.56 MHz similar in nature to previous work [13, 14]. Note the formation of the Lamb dips at the transition frequencies (transition wavelengths plotted in Table 1). Subtracting this spectra from the Doppler-broadened spectra (which is given in the absence of a pump laser) gives what is known as the Lamb peak spectra shown in Fig. 3.

2.2 The general absorption coefficient

As with all absorption spectra, Doppler-free saturated absorption spectra are obtained by plotting the absorption coefficient of the laser as it passes through the plasma versus

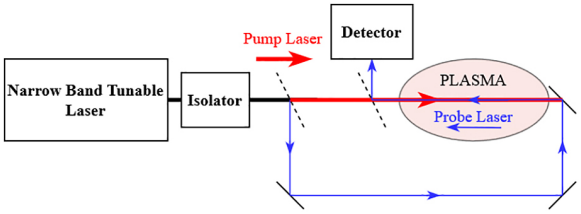

Fig. 1. A simplified schematic of experimental apparatus showcasing the pump and probe laser beams entering the plasma from opposite sides along the same axis. A more detailed schematic can be found in previous works [13, 14].

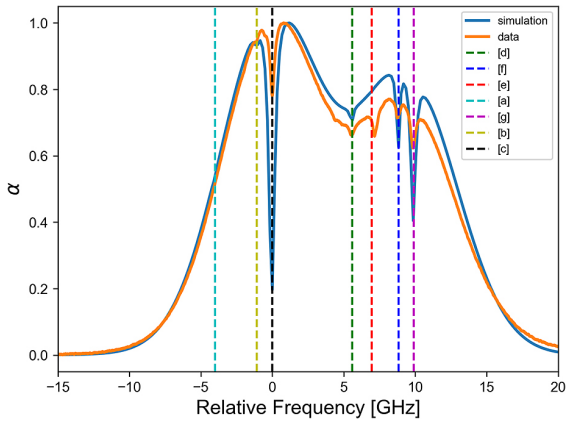

Fig. 2. Comparison between experimental data and simulated Doppler-free absorption spectra.

Table 1. The seven hydrogen Balmer-α fine structure transition lines, along with their corresponding wavelengths in nanometers and relative frequencies centered around transition [c]. Each transition will be referred to in the subsequent figures by the label given in the Key column.

Lower–Upper	λ (nm)	Rel. Freq. (GHz)	Key
$2P_{3/2} - 3S_{1/2}$	656.2909	−4.0143	[a]
$2P_{3/2} - 3D_{3/2}$	656.2867	−1.0853	[b]
$2P_{3/2} - 3D_{5/2}$	656.2852	0.0000	[c]
$2S_{1/2} - 3P_{1/2}$	656.2771	5.5823	[d]
$2P_{1/2} - 3S_{1/2}$	656.2752	6.9554	[e]
$2S_{1/2} - 3P_{3/2}$	656.2725	8.8321	[f]
$2P_{1/2} - 3D_{3/2}$	656.2710	9.8844	[g]

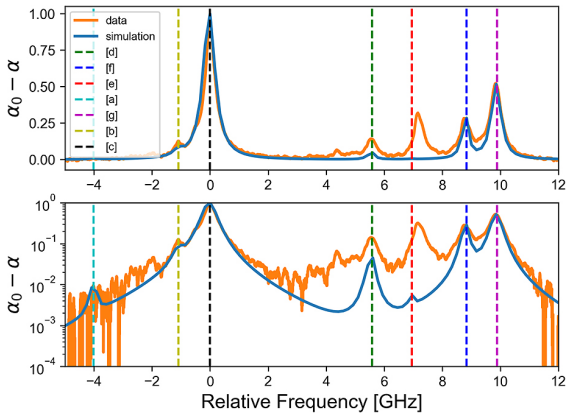

Fig. 3. (a) Comparison between experimental and modeled Lamb peak spectra. (b) Log plot of experimental and simulated Lamb peak spectra.

that same laser's frequency. The absorption coefficient can be calculated at discrete wavelengths as the laser is scanned, allowing for the derivation of the absorption spectrum over the entire profile.

In order to successfully model the spectra resulting from this experimental technique, we must be able to accurately simulate the measured absorption coefficient. This makes the plotting of the absorption coefficient versus laser frequency the goal of our simulations. Briefly put, the frequency scanning of the laser can be simulated by integrating over the particle velocity distribution for a single frequency and then repeating this integration process for every frequency value within the range of the scan to obtain the absorption coefficient at each scanned frequency. Due to the high temperature of the medium in this work the studied line profile has been broadened by the Doppler effect as well as other intrinsic broadening effects, such as natural broadening, that must be taken into account in order to accurately model Lamb dips within the Doppler-free spectra.

It is well understood that the absorption coefficient of a laser beam sent through a mono-atomic plasma at a particular frequency λ corresponding to an electron energy transition from lower state $|p\rangle$ to upper state $|q\rangle$ can be derived from the difference in the Einstein absorption coefficients of the two levels in the following manner:

$$\alpha_\lambda^i(\upsilon)d\upsilon = \frac{h\rho}{\lambda}[B(p,q)n_\upsilon(p) - B(q,p)n_\upsilon(q)]P_{\mathrm{L}}\Delta\lambda d\upsilon, \tag{1}$$

where $\alpha_\lambda^i(\upsilon)d\upsilon$ is the absorption coefficient of the probe laser light λ for a single transition i corresponding to energy levels $|p\rangle$ and $|q\rangle$ due to the group of particles projected along the laser propagation direction with velocity υ, $B(p,q)$ is the Einstein coefficient of absorption for a transition from $|p\rangle$ to $|q\rangle$, $B(q,p)$ is the Einstein coefficient of stimulus radiation from $|q\rangle$ to $|p\rangle$, $n_\upsilon(p)d\upsilon$ and $n_\upsilon(q)d\upsilon$ are the population density of levels $|p\rangle$ and $|q\rangle$ within velocity width $d\upsilon$ respectively, P_L is the intrinsic broadening distribution, ρ is the laser power density, and $\Delta\lambda$ is the laser wavelength width, where both the laser power density and wavelength width are assumed to be constant.

Note that the Einstein coefficients $B(p,q)$ and $B(q,p)$ in Eq. (1) are also constants. The velocity distributions are therefore encoded into the population density distributions from which $n_\upsilon(p)$ and $n_\upsilon(q)$ are determined for a given υ, as will be explained in further detail in the discussion of the model in the subsequent section.

We should also note that this model will ignore cross-over resonances. As will be discussed in Sec. 5.1, due to a lack of J-resolved electron collisional excitation data some assumptions regarding the population densities of the J-resolved energy levels had to be made, which in turn meant that the interference between the studied transitions could not be modeled accurately and as such were not included. There is, however, nothing preventing their inclusion in this theory as long as the relevant atomic data is obtained.

Having now laid the basic framework for obtaining the general absorption coefficient, Sec. 3 will detail how we go about obtaining the $n_\upsilon(p)$ and $n_\upsilon(q)$ terms and the P_L term from Eq. (1), and Sec. 4 will go in depth as to how the CR model is used to obtain the necessary J-resolved energy levels to resolve the $n_\upsilon(p)$ and $n_\upsilon(q)$ terms used in Sec. 3.

3. Spectra Model

3.1 Encoding the velocity distribution

To determine exactly how the velocity distributions are included in the model let us look first at the population densities of the energy levels. The particles in the plasma are assumed to have a velocity distribution, meaning that we can rewrite the total population density as

$$n_\upsilon(1)d\upsilon = N_0 P_{\mathrm{D}}(\upsilon)d\upsilon, \tag{2}$$

where N_0 and $P_D(\upsilon)$ are the total atom density and the Maxwell-Boltzmann distribution function (a result of the Doppler-broadening), respectively [15]. The product of the two, $n_\upsilon(1)d\upsilon$, is referred to as the ground state atom density within a velocity width $d\upsilon$. Focusing for now on a particular transition line i of wavelength λ_0 that corresponds to a transition between levels $|p\rangle$ and $|q\rangle$, if we wish to obtain the population density of levels $|p\rangle$ and $|q\rangle$ having velocity υ in the ensemble $n_\upsilon(1)d\upsilon$, a similar process to Eq. (2) is used

$$\begin{aligned} n_\upsilon(p)d\upsilon &= r(p)n_\upsilon(1)d\upsilon, \\ n_\upsilon(q)d\upsilon &= r(q)n_\upsilon(1)d\upsilon, \end{aligned} \tag{3}$$

where $r(p)$ and $r(q)$ are the fractions of the population of particles relative to $n_\upsilon(1)$ with lower and upper energy levels $|p\rangle$ and $|q\rangle$.

The actual values for $r(p)$ and $r(q)$ are given by the CR model addressed later on in Sec. 4. Note that when we integrate over velocity, explicit expressions for $n_\upsilon(p)$ and $n_\upsilon(q)$ are necessary.

And so, in order to obtain the total spectra we must take into account all of the particles within the medium and not just a particular subset of those with velocity υ. The total absorption coefficient is obtained by integrating Eq. (1) over υ and takes the form

$$\begin{aligned} \alpha_i(\lambda) &= \int \alpha_\lambda^i(\upsilon)d\upsilon \\ &= \int \frac{h\rho}{\lambda}[B(p,q)n_\upsilon(p) \\ &\quad - B(q,p)n_\upsilon(q)]P_{\mathrm{L}}\Delta\lambda d\upsilon. \end{aligned} \tag{4}$$

It is important to reiterate here that when the integration is carried out to obtain the total absorption coefficient, explicit expressions for $n_\upsilon(p)$ and $n_\upsilon(q)$ are necessary.

Note that the inclusion of an intrinsic broadening distribution P_{L} in Eq. (1) means that the function will not trivialize into a delta function upon integration, meaning that we cannot simplify this equation further without additional assumptions about P_{L}.

3.2 P_{L} term

The P_{L} term was rather generally introduced in Sec. 2.1 as the intrinsic broadening term. This term can be used as a catch-all for the various mechanisms in which a line can be broadened that are not captured by the physics of the CR model, as once the spectra becomes Doppler-free these other types of line broadening that were previously overshadowed and hidden by Doppler broadening can now be properly observed [16, 17]. As such, P_{L} can include terms for natural broadening, broadening via electron density, phase-interrupting or interatomic collisional broadening, or Stark broadening processes, for example. It should be mentioned that saturation broadening is deliberately not included in this term, as this specific type of broadening arises naturally out of the inclusion of an optical pumping term in the CR model, as will be explained in Sec. 4. With respect to the P_L term in this work, we will ignore everything except the natural line width and solely use the P_{L} term to denote natural line broadening, described simply with a Lorentzian distribution. Specific additions to the physics of this work, such as the inclusion of Stark broadening, would therefore require adjusting the P_{L} term to include these phenomena. However, the following description of the P_{L} term will remain relevant even in such scenarios.

By virtue of having broadened transition lines, even when the laser wavelength is different from the central wavelength of the absorption coefficient profile λ_0, there exist some particles that will absorb the laser light. As was explained in Sec. 2.1, the reference point of a particle with velocity υ parallel to the laser axis would see the lasers at different wavelengths λ_υ, with the strength of this shift depending on υ in accordance to Doppler shifting:

$$\lambda_\upsilon = \lambda_0\left(1 - \frac{\upsilon}{c}\right), \tag{5}$$

where λ_0 is the wavelength of the light absorbed by particles at rest.

This means that the amount of the natural broadening due to the particles with velocity υ is dependent on the difference between the shifted wavelength due to the particles of speed υ, λ_υ, and the laser wavelength from an inertial reference frame, λ. As such the natural broadening distribution for a given υ would be a Lorentzian distribution centered at $(\lambda_\upsilon - \lambda)$

$$P_{\mathrm{L}} = \frac{1}{\pi}\frac{\gamma/2}{(\lambda_\upsilon - \lambda)^2 + (\gamma/2)^2}, \tag{6}$$

where full width at half maximum (FWHM) γ is simply given by the natural broadening width. To keep notation consistent, the P_{L} term in the α equations can be written as $P_{\mathrm{L}}(\lambda_\upsilon - \lambda)$, where λ is the probe laser wavelength, whereas the P_{L} terms in CR model, which we will see in Sec. 4 can be written generally as $P_{\mathrm{L}}(\lambda_{qp}(1 - \frac{\upsilon}{c}) - \lambda_{\mathrm{pump}})$ and $P_{\mathrm{L}_{jk}}$ as $P_{\mathrm{L}_{jk}}(\lambda_{q_j p_k}(1 - \frac{\upsilon}{c}) - \lambda_{\mathrm{pump}})$ for the J-resolved levels, with λ_{qp} and $\lambda_{q_j p_k}$ as the specific wavelengths associated with the transitions from $|q\rangle$ to $|p\rangle$ and from $|q_j\rangle$ to $|p_k\rangle$ respectively, and λ_{pump} being the pump laser wavelength. This notation is used in the CR model to draw attention to the fact that the P_{L} and $P_{\mathrm{L}_{jk}}$ terms are dependent on $\lambda_{qp}$and $\lambda_{q_j p_k}$ respectively, as well as on the pump laser wavelength and not the probe laser wavelength.

4. Collisional-Radiative Model

As stated previously, the CR model is used to obtain values of $r(p)$ and $r(q)$ for the energy levels $|p\rangle$ and $|q\rangle$ to be used within the particle groups $n_\upsilon(p)$ and $n_\upsilon(q)$ in explicitly solving for the absorption spectra $\alpha(\lambda)$. The CR model used in the following calculations is tailored specifically for hydrogen atoms. Simply put, the basic assumption of the CR model is that the particle populations in each energy level are in equilibrium states.

$$\frac{d}{dt}r(p) = \Gamma_{\mathrm{in}} - \Gamma_{\mathrm{out}} = 0, \tag{7}$$

where Γ_{in} stands for the sum of all of the collisional and optically allowed radiative transitions in which a particle may enter level $|p\rangle$ from any level $|q\rangle$, and Γ_{out} is all of the collisional and optically allowed radiative transitions in which a particle may exit level $|p\rangle$ into any level $|q\rangle$ [18]. We thus create a system of equations using Eq. (7) for each level $|p\rangle$ excluding the ground state.

Without the existence of a pump laser the equations for Γ_{in} and Γ_{out} can be written as

$$\Gamma_{\mathrm{in}} = \sum_q C(q,p)n_e r(q) + \sum_{q>p} A(q,p)r(q), \tag{8}$$

and

$$\Gamma_{\mathrm{out}} = \sum_q C(p,q)n_e r(p) + \sum_{q<p} A(p,q)r(p) + S(p)n_e r(p), \tag{9}$$

respectively, with $C(q,p)$ being either the excitation or de-excitation rate coefficients for the transitions from $|q\rangle$ to $|p\rangle$ due to electron collisions, $A(q,p)$ being the Einstein coefficients for spontaneous radiation from $|q\rangle$ to $|p\rangle$, $S(p)$ referring to the ionization rate coefficient for level $|p\rangle$, and n_e as the electron density. The model includes all of the $|nL\rangle$ levels from $n = 1$ to $n = 4$, where n is the principle quantum number and L is the orbital angular momentum quantum number. The coupled equations are then solved and the particle population distributions per velocity interval are obtained. Note that recombination processes are ignored in the current iteration of this model.

4.1 Pump laser term

By turning the pump laser on we introduce induced transitions into both equations. Just like with the equations for the absorption coefficient, the wavelength of the pump laser light absorbed by a group of particles can also be shifted according to the corresponding projection velocity of the particles in that group. This once again necessitates the inclusion of an intrinsic broadening term P_{L} in the CR model. The effect of optical pumping on the saturation of particle population densities is well studied, and the inclusion of such a term into the CR model will inherently lead to saturation

broadening of the Lamb dips produced by the model [1]. With this in mind, we can update the CR model to include the pump laser term along with the optical pumping term,

$$\Gamma_{\text{in}} = \sum_q C(q,p)n_e r(q) + \sum_{q>p} A(q,p)r(q) + \sum_q B(q,p)r(q)P_{\text{L}}\rho\Delta\lambda, \tag{10}$$

and

$$\Gamma_{\text{out}} = \sum_q C(p,q)n_e r(p) + \sum_{q<p} A(p,q)r(p) + S(p)n_e r(p) + \sum_q B(p,q)r(p)P_{\text{L}}\rho\Delta\lambda\,. \tag{11}$$

Note that there is again dependence on υ in the intrinsic broadening term P_{L}. The nature of this dependence is identical to that discussed in Sec. 3.2. This denotes that the central peak of the intrinsic broadening is dependent on the velocity group υ. This means that the CR model must be run independently for each discrete value of υ in our model and explains why the values $n_\upsilon(p)$ and $n_\upsilon(q)$ must be solved explicitly during integration.

The nature of the CR model allows for additional methods of particle excitation and de-excitation to be easily added into the equations for Γ_{in} and Γ_{out} as extra terms, which, much like the P_{L} term allows for an extremely flexible structure that can accommodate all manner of particle excitation and de-excitation methods and effects.

4.2 *J*-resolved energy levels

Up until this point the CR model we have outlined has solely dealt with the assumption that the energy levels used were $|nL\rangle$ levels, where a fixed $S = 1/2$ is implicitly assumed. This is largely due to the fact that the data obtained for use in this iteration of the CR model is not based on levels $|nLJ\rangle$, but on levels $|nL\rangle$, where J is the quantum number of the total angular momentum [19].

However, it is possible to extrapolate data from the J-resolved levels without explicitly knowing the necessary cross-sectional data needed to calculate the Einstein coefficients nor the excitation and de-excitation coefficients associated with these J-resolved levels, as long as we can assume that the particle population ratio between the J-resolved energy levels are at equilibrium and mirror their respective statistical weight ratios. We assume that interatomic collisions are infrequent and that the J-level population distribution follows the statistical weight due to inelastic electron-atom collisions. We consider the former assumption reasonable as Lamb dips have actually been observed, and the latter because the relative depth of each observed Lamb dip roughly agrees with the calculation results. In the future, we intend to construct resolved in J-levels to allow for more detailed analysis.

This would necessitate that the electron density of the plasma would have to be high enough such that the inelastic electron-atom collisions happen consistently enough to maintain their respective statistical weight ratios, which puts a lower bound on the total electron density of the plasma that the model is able to simulate. Once the electron density of the plasma reaches an order of approximately 10^{16} m^{-3} this condition no longer holds for hydrogen plasma.

Consider a laser-induced transition from $|q\rangle$ to $|p\rangle$. Let us assume that $|q\rangle$ has two J-resolved energy levels $|q_1\rangle$ and $|q_2\rangle$ and $|p\rangle$ consists of $|p_1\rangle$ and $|p_2\rangle$ J-resolved levels. When a laser light with the wavelength corresponding to the transition from $|q_1\rangle$ to $|p_1\rangle$ is introduced, it is supposed that only a fraction of the $|q\rangle$ level, which is evaluated by the statistical weights of relevant levels, can be excited to the $|p\rangle$ level. The actual transition coefficient can be expressed by including the ratio of the statistical weights of the relevant levels $B(q_1, p_1)g(q_1)/g(q)$.

Thus, if level $|p\rangle$ has k J-resolved levels and $|q\rangle$ has j J-resolved levels, we can sum through all k and j J-resolved levels for a transition involving a given $|p\rangle$ and $|q\rangle$ to include natural broadening that is dependent on the specific $|q_j\rangle$ to $|p_k\rangle$ J-resolved transition wavelength (which are well known for Balmer-α) while maintaining the same mathematical total in the pump laser induced transition terms in the CR model.

$$\sum_q B(q,p)P_{\text{L}} = \sum_q \sum_{j,k} \frac{g(q_j)}{g(q)} B(q_j, p_k)P_{L_{j,k}}. \tag{12}$$

With $\frac{g(q_j)}{g(q)}$ being the aforementioned statistical weight ratio of the J-resolved level $g(q_j)$ to the total weight of level $|q\rangle$, $g(q)$.

We can then substitute in the J-resolved inclusive summation for the averaged transition term in the induced radiation section for both equations Γ_{in} and Γ_{out}.

$$\Gamma_{\text{in}} = \sum_q C(q,p)n_e r(q) + \sum_{q>p} A(q,p)r(q) + \sum_q \sum_{j,k} \frac{g(q_j)}{g(q)} B(q_j, p_k)r(q)P_{\text{L}_{j,k}}\rho\Delta\lambda, \tag{13}$$

and

$$\Gamma_{\text{out}} = \sum_q C(p,q)n_e r(p) + \sum_{q<p} A(p,q)r(p) + S(p)n_e r(p) + \sum_q \sum_{j,k} \frac{g(p_k)}{g(p)} B(p_k, q_j)r(p)P_{\text{L}_{j,k}}\rho\Delta\lambda\,. \tag{14}$$

With the equations for Γ_{in} and Γ_{out} obtained in full we can now substitute them into Eq. (7) to solve for the populations of the desired energy levels. In this work we are interested mainly in the Balmer-α lines, so the J-resolved levels being taken into consideration are the resultant seven transitions which can be seen as the dotted lines in Figs. 2 to 12. In this work we included energy levels from the ground state up to 4F, although the pump laser term was only included in levels associated with the Balmer-α line. As such, we ended up with a linear system of nine equations, which were subsequently solved for a given υ to obtain the J-resolved energy levels used in the $\alpha(\lambda)$ calculations.

4.3 Multiple transition lines

Before discussing the results, let us quickly mention how we would go about solving for the absorption spectra of multiple transition lines simultaneously. We make use of the superposition principle for these spectra. For a multitude of transition lines i,

$$\alpha(\lambda) = \sum_i \alpha_i(\lambda) = \sum_i \left(\frac{h\rho N_0}{\lambda} [B(p_i, q_i) r(p_i) \Delta\lambda - B(q_i, p_i) r(q_i)] \int P_{L_i}(\lambda_v - \lambda) P_D(v) dv \right), \quad (15)$$

where λ_i is simply the central wavelength λ_0 for the specific transition i.

Note that this does not necessitate recalculating the values of $n_v(p)$ and $n_v(q)$ for each transition i, since the CR model carries the information of all the transitions you wish to look at in order to determine the particle population at any given level, as long as simultaneous calculations of the energy level populations are carried out, there is no need to iterate the CR model system of equations over i.

5. Results and Discussion

5.1 CR model output

Having discussed in length the theory behind the CR model, let us now discuss how we obtained the atomic data used in it. The model was constructed in Python and uses atomic data assembled by Sawada [20]. The Einstein A and B coefficients are derived with the formula given in [18] where the radial components of the wavefunction are calculated following the method described in Ref. [21]. The cross-section data for electron collision excitation and ionization

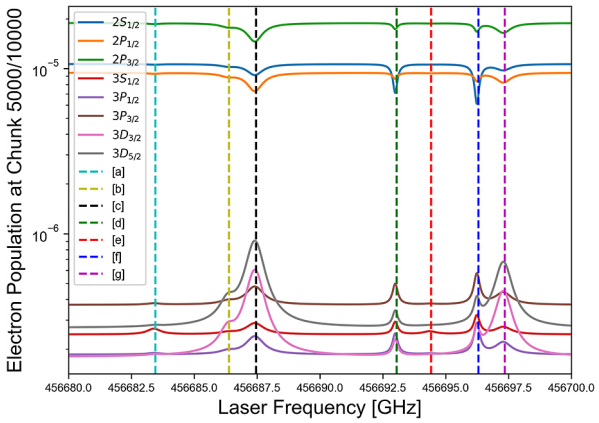

Fig. 4. Plot of the N = 2 & 3 J-resolved energy level populations vs frequency at the center of the particle velocity distribution (denoted as chunk 5,000 out of 10,000). Note that there is slight influence on every energy level population at each transition frequency, but this influence becomes noticeably more pronounced with energy levels associated with a particular transition. Particularly of note is the shared influence between J-resolved energy levels that share the same $|nL\rangle$.

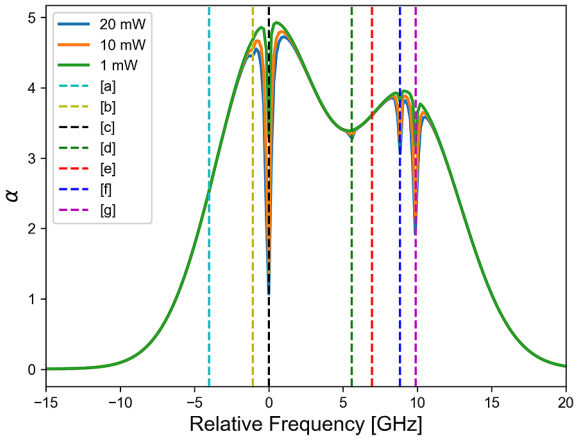

Fig. 5. A comparison of the Doppler-free absorption spectra $\alpha(\lambda)$ as the laser power is changed from 1 to 20 mW.

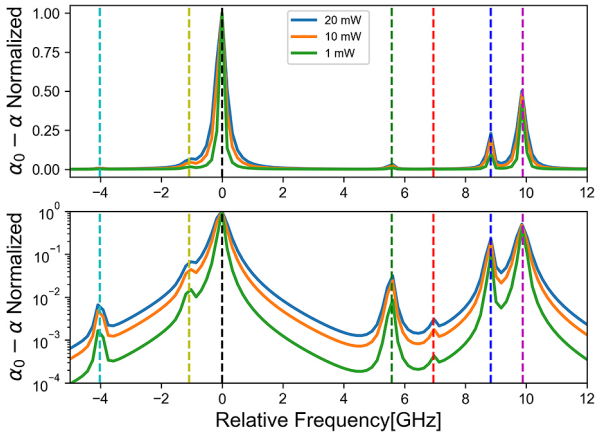

Fig. 6. (a) A comparison of the Lamb peaks of the spectra in Fig. 5 as the laser power is changed. Note the increasing width as the laser power increases. (b) A log plot of the Lamb peaks that further showcases the increase in Lamb width as the laser power increases.

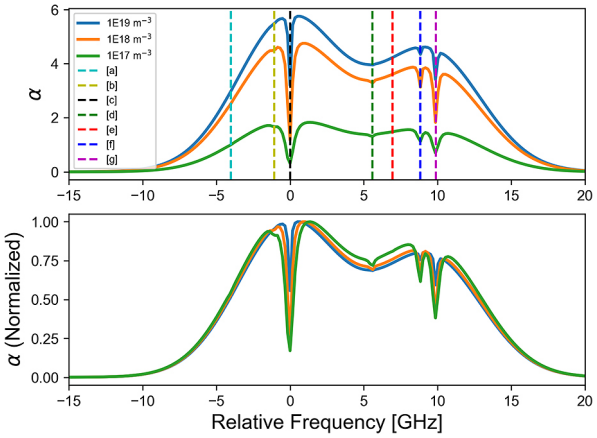

Fig. 7. (a) A comparison of the Doppler-free absorption spectra $\alpha(\lambda)$ as the electron density is changed from 10^{17} m^{-3} to 10^{19} m^{-3}. (b) A normalized comparison of the absorption spectra $\alpha(\lambda)$ as the electron density is changed, showcasing how the Lamb dip depth ratio is affected by the electron density.

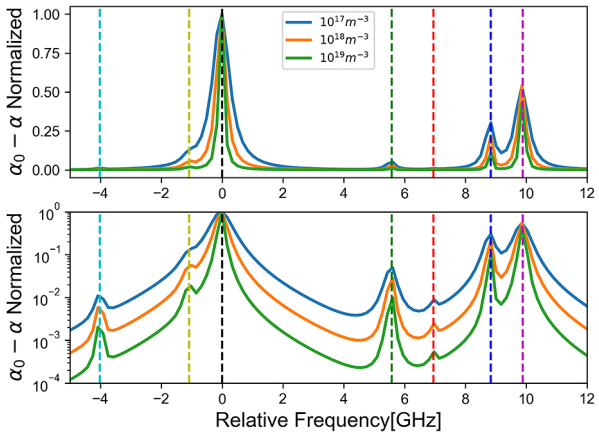

Fig. 8. (a) A comparison of the Lamb peaks of the spectra in Fig. 7 as the electron density is changed. Note the increasing width as the electron density decreases. (b) A log plot of the Lamb peaks that further showcases the decrease in Lamb width as the electron density increases.

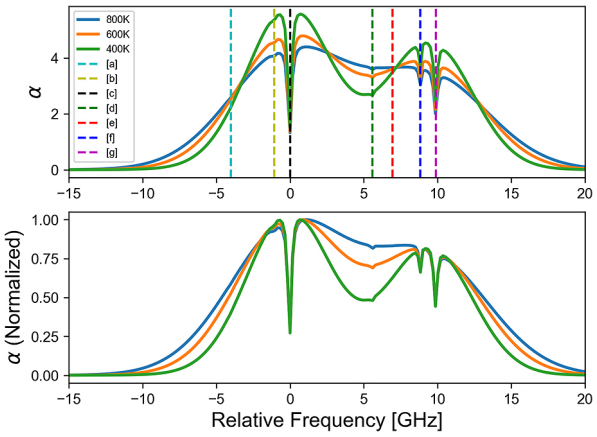

Fig. 9. (a) A comparison of the Doppler-free absorption spectra $\alpha(\lambda)$ as the atom temperature is from 400 to 800 K. (b) A normalized comparison of the absorption spectra $\alpha(\lambda)$ as the atom temperature is changed from 400 to 800 K, showcasing the lack of impact the atom temperature has on the depth ratio of the Lamb dips.

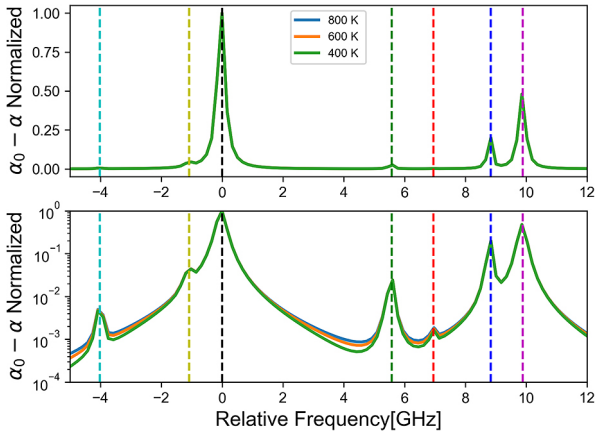

Fig. 10. (a) A comparison of the Lamb peaks of the spectra in Fig. 9 as the atom temperature is changed. (b) A log plot of the Lamb peaks that shows no broadening of the Lamb peaks as the atom temperature increases.

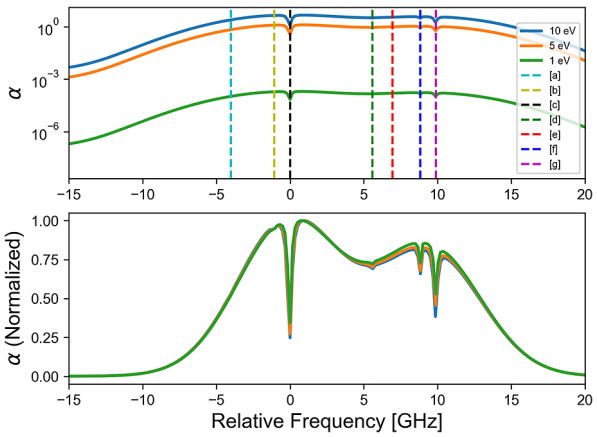

Fig. 11. (a) A log plot comparing the Doppler-free absorption spectra $\alpha(\lambda)$ as the electron temperature is changed from 1 to 20 eV. (b) A normalized comparison of the absorption spectra $\alpha(\lambda)$ as the electron temperature is changed from 1 to 10 eV, showcasing the minor impact the electron temperature has on the Lamb dip depth ratios.

are derived by the Born approximation [20] with the generalized oscillator strength [22], and their rate coefficients are derived with an assumption of the Maxwell velocity distribution for electrons.

We now turn to the CR model outputs used in Eq. (3) before solving for the absorption coefficient $\alpha(\lambda)$ in Eq. (4). The CR model outputs the J-resolved energy level populations for a given velocity interval and a particular laser frequency. Figure 4 gives all the energy level populations verses frequency for the central interval of the particle velocity distribution. In other words, this figure is a relation between $n_v(p)$ defined in Eq. (3) and the frequency for a given particle velocity. In this case the particle velocity is zero along the laser axis, as the velocity distribution is centered around particles moving perpendicularly to the laser axis. This means that there is no Doppler shift of the transition frequencies due to particle velocity along the axis.

As such, we can see in Fig. 4 that each of the energy

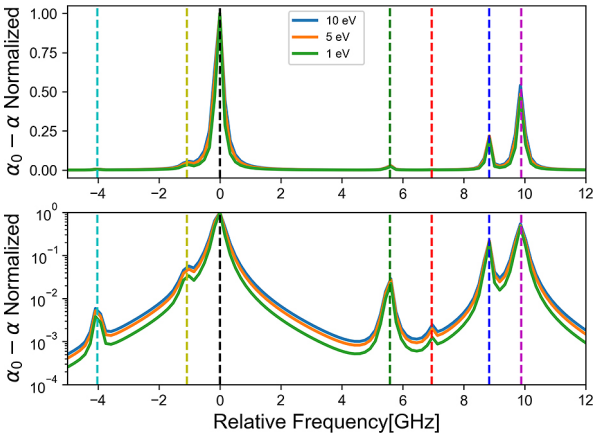

Fig. 12. (a) A comparison of the Lamb peaks of the spectra in Fig. 11 as the electron temperature is changed. (b) A log plot of the Lamb peaks that more clearly showcases the increase in Lamb width as the electron temperature increases.

level populations are influenced at each of the transition frequencies, but the influence increases when the *J*-resolved energy level corresponds to one of the energy levels associated with a particular transition frequency. This is most notable with both levels $3D_{5/2}$ and $3D_{3/2}$ seeing substantial increases in population at the gold [b], black [c], and violet [g] dotted lines, each of which is a transition involving one of these two states as the upper energy level, as shown in Table 1. The fact that both upper energy level populations are influenced at all three transition frequencies can be attributed to their shared *L*-level and the earlier assumption of the *J*-level particle populations mirroring their statistical weight ratios. As a result, any laser influence on one of these *J*-levels will invariably have some influence on the other *J*-level in order to maintain the assumed statistical balance. This behavior is precisely why crossover resonances are ignored in this work, as the laser influenced coupling of the *J*-resolved level populations resulting from this assumption does not allow for accurate crossover resonance modeling. In the future, we intend to construct a model resolved in the *J*-levels to do away with this assumption and allow for more accurately detailed evaluation in this regime.

We can see a similar pattern at the $2S_{1/2}$ level, which has pronounced drops in population at the green [d] and blue [f] dotted lines, both of which can be verified by Table 1 to contain $2S_{1/2}$ as the lower energy level of those transitions. All in all, these results show that we can expect changes in the absorption coefficient at these transition frequencies due to the effect on the particle population levels of the transitions associated with their respective transition frequencies.

5.2 Spectral characteristics as functions of plasma parameters

Before we move on, it is necessary to discuss certain parameter values used in the following simulations. A constant laser beam cross section of 10^{-4} m^2 with a laser width of 3×10^5 Hz was assumed for the duration of the scan. The laser width additionally dictated the corresponding step size in the velocity domain, as the laser beam with a given thickness $\Delta\lambda$ could only ever correspond to a single particular velocity group of thickness Δv within the distribution.

The seven fine structure components of the hydrogen Balmer-α line referenced in the following figures are listed in Table 1.

The parameter α denotes the spectra as given by Eq. (15), with α_0 denoting the unmodified Doppler-broadened spectra given by the equation

$$\begin{aligned}\alpha_0(\lambda) &= \sum_i \alpha_0^i(v)dv \\ &= \sum_i \left(\frac{hv}{c}[B(p_i, q_i)n_{\alpha 0}(p_i) \right. \\ &\quad \left. - B(q_i, p_i)n_{\alpha 0}(q_i)]P_D(v)\right),\end{aligned} \tag{16}$$

where $n_{\alpha 0}(p_i)$ and $n_{\alpha 0}(q_i)$ are the results of the CR model for a given $|p\rangle$ and $|q\rangle$ corresponding to a transition i with the optical pumping term given in Eq. (12) set to zero. These terms are, in essence, the Doppler-broadened equivalents to $n_v(p)dv$ and $n_v(q)dv$ in Eq. (2). Plotting the difference $\alpha_0 - \alpha$ highlights the resultant "Lamb peaks" and allows for more accurate analysis, as can be seen in Figs. 3, 6, 8, 10, and 12.

5.2.1 Laser power

Let us now take a look at how the notable spectral characteristics can be seen as functions of certain plasma parameters, beginning with the dependence on the laser power. Figure 5 plots the absorption spectra $\alpha(\lambda)$ for varying laser powers, from 1 to 20 mW. All other plasma parameters were held constant between these three simulations, with the atom temperature set at 600 K, electron temperature at 10 eV, and the electron density at 10^{18} m^{-3}. Figure 5 demonstrates a clear relationship between Lamb dip length and Laser power, with the depth of the Lamb dips increasing as the laser power is increased.

Figure 6 plots the normalized Lamb peaks of the three spectra shown in Fig. 5, with the bottom graph being the log of the Lamb peaks in order to better showcase the differences in between the three Lamb peak spectra. Here we can see a clear relation between the Lamb peak width and the laser power, as the increase in laser power serves to increase the amount of optical pumping and, by extension, saturation broadening of the Lamb peaks.

5.2.2 Electron density

Let us now look at the electron density dependence. We ran simulations for electron densities ranging from 1×10^{17} to 1×10^{19} m^{-3}, the laser power set to 15 mW with all other plasma parameters held constant as detailed in the previous subsection. Electron density dependence can be explicitly seen in the parameter n_e seen in Eqs. (10) and (11) within the CR model. This means that the values of $n_v(p)$ and $n_v(q)$ seen in Eq. (4), and thus in turn $\alpha(\lambda)$, have an explicit dependence on the electron density.

Looking at Fig. 7(a) we can see that as electron density increases, the overall structure of the spectra is maintained, but overall height of the spectra increases dramatically. Upon close inspection of Fig. 7(b) one can note that the depth ratio of Lamb dip to the max height of the spectra decreases as the electron density increases. In other words, the ratio of the max height of the spectra to the depth of the Lamb dips decreases as the electron density increases.

Figure 8 shows that as the electron density increases, we see a decrease in the width of the Lamb peaks. Inversely, the Lamb peaks broaden as the electron density decreases. This rather curious phenomenon we believe can be explained due to saturation broadening, otherwise known as power broadening, which will be expounded on further in a future paper.

5.2.3 Atom temperature

Figure 9(a) plots the absorption spectra for various atom temperature ranging from 400 to 800 K. As is confirmed by Fig. 10, there is practically no change at all to the overall shape of the Lamb dips/peaks, aside from extremely slight broadening of transitions [d] and [e] in the center of the spectra and transition [a] on the left, although on an order small enough that would most likely not be detectable by experiments.

Both the absolute lack of dependence of the Lamb dip depth ratio shown in Fig. 9(b) and the minuscule amount of change in the Lamb peak broadening in Fig. 10 due to the atom temperature is a clear sign that the saturation parameter is in no way dependent on the atom temperature. Instead, we see clear dependence of the atom temperature on the Doppler-broadened spectra shape and width in Fig. 9(a). The Doppler-broadened spectra is dependent on the defined most probable speed, which is itself proportional to square root the atom temperature, whereas the Lamb dips themselves are independent of the Doppler-spectral parameters.

5.2.4 Electron temperature

The normalized plot of $\alpha(\lambda)$ for a range of electron temperatures from 1 to 10 eV shown in Fig. 11(b) shows that the Lamb dip ratio increases with electron temperature. The figure also demonstrates a slight suppression in the height of secondary Doppler-broadened bump associated with transitions [f] and [g].

Figure 12 shows that varying the electron temperature has a slightly larger impact on Lamb peak width than varying the atom temperature, however its impact on Lamb peak broadening is still considerably lesser then that of either the laser power or the electron density dependence.

5.3 Comparison with experiment

With the relationship between these parameters having been shown in the previous subsections, it is possible to use these relationships to compare the constructed model with experimentally taken data. The experimental data shown in Figs. 2 and 3 were taken for an ICP source [13, 14].

The given experimental parameters in these figures are a laser power of 18.6 mW, an atom temperature of about 600 K and an electron temperature of approximately 10 eV. The electron density is estimated to be on the order of 10^{18} m^{-3}. The graphed simulation took on the values of the best estimations for the experimental atom and electron temperature at 600 K and 10 eV, as did the simulated electron density with a value of 10^{18} m^{-3}. The exception was the simulated laser power, which was modeled at 18 mW instead of the experimental value of 18.6 mW.

As shown in Figs. 2 and 3, when the model is given these parameter values, the resultant spectra (plotted in blue for Figs. 2 and 3) have generally good agreement with the experimental data (given in orange in both figures), with some over and undershooting of the Lamb dip magnitudes in Fig. 2 but particularly good agreement with respect to the locations and width of the lamb dips in Fig. 3. In addition the experimental spectrum contains some extraneous peaks in the 2.5 to 7.5 GHz range that are not captured by the model (noting again that the x-axis in both graphs is relative to transition [c] given in Table 1).

A number of these extraneous peaks seen in the experimental spectrum of Fig. 3 that are not represented in the simulation are well understood to be the result of cross-over resonance as some of the seven studied transitions share the same lower energy level. This cross-over resonance causes population fluctuations in a given transition's upper energy level to affect the particle population of other upper energy levels whose transitions 'share' a lower energy state with the aforementioned upper energy level. The influence of this cross-over resonance can therefore be found at exactly halfway between the frequencies of the two transitions in question. The most easily seen of these crossover resonances in the experiment is the large peak slightly off center from transition [e] in Fig. 3, whose peak position corresponds to halfway between transitions [d] and [f] at roughly 7.2 GHz relative to transition [c], matching exactly with the center of the experimental peak near transition [e]. We do not see these peaks in the simulation as the current iteration of the model does not account for these types of resonances between population levels.

Explanations for the discrepancy in the experimental and simulated Lamb dip depth ratios in Fig. 2 are less intuitive, but nonetheless are still important to consider. One possible candidate comes from the model's current lack of implementation of momentum transfer collisions that would allow for particles to move between the velocity intervals discussed in Sec. 3.2. Accounting for such momentum transfer collisions could in theory serve to 'replenish' the amount of particles at a given transition's lower energy level, counteracting the saturation effect of the pump laser and increasing the absorption of the probe laser to potentially better match that of the experiment at these transition frequencies. Of course it is possible that there are multiple effects at play here not currently accounted for in the model that are contributing to this discrepancy in the Lamb dip depth ratio in addition to the current lack of inclusion of momentum transfer collisions in the model.

6. Conclusion

In conclusion, our technique is able to successfully model Doppler-free spectra, showcasing that its theoretical base looks to be sound. Given plasma parameters similar to those recorded experimentally, the model effectively simulates the resultant experimental spectrum. The inconsistencies in the model's spectra have been shown to be encouragingly minor and are mainly due to various atomic effects not having been included in the current iteration of this model and can therefore be rectified with further iteration.

This model has helped showcase further insight into how plasma parameters such as electron density, laser power, and atom and electron temperature can affect the spectral characteristics of Lamb dips such as their shape, depth, width, and ratio between dips. More specifically, we have shown that the laser power, electron density, and electron temperature all play a direct role in both the depth and width of the spectral Lamb dips due to the dependence of the particle saturation on these plasma parameters, whereas atom temperature had demonstrably no effect on the saturation. Continuing to focus our attention on modeling the spectral characteristics of Lamb dips in this manner will only serve to

grant further insight into plasma parameters and atomic processes within all sorts of plasma.

[1] W. Demtröder, *Laser Spectroscopy*, 4th edition (Springer-Verlag, Berlin, Heidelberg, 2008).
[2] S. Welzel *et al.*, Plasma Sources Sci. Technol. **16**, 822 (2007).
[3] J. Röpcke *et al.*, Plasma Sources Sci. Technol. **15**, S148 (2006).
[4] M. Aramaki *et al.*, Jpn. J. Appl. Phys. **44**, 6759 (2005).
[5] A. Rousseau *et al.*, Plasma Sources Sci. Technol. **13**, 166 (2004).
[6] H. Scheibne *et al.*, Rev. Sci. Instrum. **73**, 378 (2002).
[7] M. Hiramatsu *et al.*, Meas. Sci. Technol. **2**, 1017 (1991).
[8] B.W. Petley *et al.*, J. Phys. B **13**, 3099 (1980).
[9] E.W. Weber, Phys. Rev. A **20**, 2278 (1979).
[10] E.W. Weber and H.J. Humpert, Phys. Lett. A **83**, 386 (1981).
[11] E.W. Weber *et al.*, Appl. Phys. B **32**, 63 (1983).
[12] R. Asakawa *et al.*, J. Instrum. **7**, C01018 (2012).
[13] S. Nishiyama *et al.*, Appl. Phys. Express **10**, 036101 (2017).
[14] S. Nishiyama *et al.*, J. Phys. D: Appl. Phys. **50**, 234003 (2017).
[15] A. Thorne *et al.*, *Spectrophysics: Principles and Applications*, (Springer-Verlag, Berlin, Heidelberg, 1999).
[16] A. Zafar *et al.*, J. Quant. Spectrosc. Radiat. Transf. **230**, 48 (2019).
[17] N. Sadeghi and M. Goto, J. Quant. Spectrosc. Radiat. Transf. **245**, 106875 (2020).
[18] T. Fujimoto, *Plasma Spectroscopy*, International Series of Monographs on Physics (Oxford University Press, Oxford, 2004).
[19] K. Sawada and T. Fujimoto, Phys. Rev. E **49**, 5565 (1994).
[20] K. Sawada, Ph.D. Thesis, (Kyoto University, Kyoto, 1994).
[21] E.U. Condon and G.H. Shortley, *The Theory of Atomic Spectra* (Cambridge University Press, Cambridge, 1959).
[22] I. Shimamura, J. Phys. Soc. Jpn. **30**, 824 (1971).